

Unraveling the non-equilibrium chemistry of the temperate sub-Neptune K2-18 b

A. Y. Jaziri^{1,2}, O. Sohier¹, O. Venot³ and N. Carrasco^{1,4}

¹ LATMOS/IPSL, UVSQ Université Paris-Saclay, Sorbonne Université, CNRS, Guyancourt, France

² Laboratoire d'astrophysique de Bordeaux, Univ. Bordeaux, CNRS, B18N, allée Geoffroy Saint-Hilaire, 33615 Pessac, France

³ Université Paris Cité and Univ Paris Est Creteil, CNRS, LISA, F-75013 Paris, France

⁴ ENS Paris-Saclay, Université Paris-Saclay, Gif-sur-Yvette, 91190, France

Received 12 May 2025; accepted 17 July 2025

ABSTRACT

Context. The search for habitable, Earth-like exoplanets faces significant observational challenges due to their small size and faint signals. M-dwarf stars provide an opportunity to detect and characterize smaller planets, particularly sub-Neptunes, which are among the most common exoplanetary types. K2-18 b, a temperate sub-Neptune in the habitable zone of an M-dwarf star, has been studied using HST and JWST, revealing an H₂-rich atmosphere with detected CH₄ and possible CO₂. However, previous debates in atmospheric composition, emphasize the importance of non-equilibrium chemistry models. These models are crucial for interpreting exoplanetary atmospheres, constraining key parameters such as metallicity, C/O ratio, and vertical mixing (K_{zz}).

Aims. This study aims to comprehensively explore the parameter space of metallicity, C/O ratio, and K_{zz} for K2-18 b using the non-equilibrium chemical model *FRECKLL* in conjunction with JWST observational data. By refining these constraints, we seek to improve our understanding of the planet's atmospheric composition and detect minor species in a temperate sub-Neptune within the habitable zone of an M-dwarf star.

Methods. Our approach involves running non-equilibrium chemical models across a three-dimensional parameter space (metallicity, C/O ratio, and K_{zz}), generating the corresponding theoretical spectra, and comparing these spectra to JWST observational data to refine atmospheric constraints. This approach assumes a fixed P–T profile, which is sufficient to capture first-order chemical trends, though it introduces some uncertainty in the derived values.

Results. We retrieved a best-fit atmospheric model for K2-18 b favoring high metallicity (266_{-104}^{+291} at 2σ) and a high C/O ratio ($C/O \geq 2.1$ at 2σ). CH₄ is robustly detected ($\log_{10}[\text{CH}_4] = -0.3_{-1.7}^{+0.1}$ at 1 mbar), while CO₂ and other species remain uncertain due to observational noise and spectral overlap. The K_{zz} has no significant impact on the fit and remains unconstrained. Non-equilibrium models exceed 4σ confidence over a flat-line which validates the presence of atmospheric features. Several minor species may exist at ppm levels, though their features are likely masked by dominant species.

Conclusions. We used non-equilibrium chemical models and JWST data to investigate the atmosphere of K2-18 b, revealing a high metallicity, a high C/O ratio and complex chemical composition. While CH₄ is robustly detected, CO₂ remains uncertain, and minor species like H₂O and NH₃ are likely present. A lower limit on the C/O ratio is constrained, though no upper limit is established. The high C/O ratio also suggests a higher probability of aerosol formation. Our findings highlight the limitations of traditional retrievals with constant abundances and the importance of non-equilibrium models with combining exploration on a large range of metallicity and C/O ratio. Although equilibrium models can reproduce the data, physical conditions indicate that the atmosphere is in a non-equilibrium state, highlighting the limited constraints from current observations and the pressing need for improved data. Future observations with JWST NIRSpec G395H and ELT/ANDES will be key to refining atmospheric constraints and probing potential habitability.

Key words. exoplanets - atmospheres – chemistry - K2-18 b

1. Introduction

The search for Earth-like habitable planets is challenging due to their small size and low brightness, which reduce the signal-to-noise ratio and strain current detection and characterization techniques. A few candidates have been identified by leveraging the smaller size and lower luminosity of M-dwarf stars, such as those in the TRAPPIST-1 system (Gillon et al. 2017). However, none have been confirmed to host an atmosphere detectable with current instruments.

Despite this, M-dwarf stars, which constitute the majority of stars in the galaxy, provide a unique opportunity to detect and characterize smaller exoplanets. In particular, sub-Neptunes ($1.7 R_{\oplus} < R < 3.5 R_{\oplus}$) orbiting M-dwarf stars are ideal candi-

dates for study. Their H₂-rich atmospheres result in large scale heights, leading to prominent spectral features that are more easily detectable. This remains true even for temperate sub-Neptunes such as K2-18 b (Benneke et al. 2017) and TOI-270 d (Günther et al. 2019). Sub-Neptunes are among the most commonly detected exoplanets and thus dominate the known population (Fressin et al. 2013; Luger & Barnes 2015; Owen & Mohanty 2016; Van Eylen et al. 2018; Hardegree-Ullman et al. 2019). They are particularly intriguing because they have no direct analogs in our solar system, raising fundamental questions about the processes that shape their atmospheres, interiors, formation, and potential habitability (Cabot et al. 2024). The habitability of such planets orbiting M-dwarf stars is actively being

investigated and is challenged by unique environmental conditions such as intense stellar flares, high-energy particle events, and limited ultraviolet flux (Scalo et al. 2007; Ricker et al. 2015; Shields et al. 2016; Rimmer et al. 2018).

K2-18 b is a temperate sub-Neptune orbiting within the habitable zone of an M-dwarf star. Its atmosphere was first characterized using the Hubble Space Telescope (HST) (Tsiaras et al. 2019; Benneke et al. 2019) and more recently with the James Webb Space Telescope (JWST) (Madhusudhan et al. 2023; Wogan et al. 2024; Schmidt et al. 2025). HST’s Wide Field Camera 3 (WFC3) provided a limited wavelength range (1.1–1.7 μm) to analyze the planet’s atmospheric composition. While this was sufficient to confirm an H_2 -dominated atmosphere, it was not enough to distinguish between the presence of H_2O (Tsiaras et al. 2019; Benneke et al. 2019) and CH_4 (Blain et al. 2021). JWST, with its broader wavelength coverage (0.9–5.2 μm) enabled by the combined NIRISS SOSS and NIRSpec G395H instruments, resolved this ambiguity in favor of CH_4 , detecting approximately 1% CH_4 and 1% CO_2 (Madhusudhan et al. 2023). Blain et al. (2021) had previously predicted the presence of CH_4 using disequilibrium chemistry models, emphasizing the crucial role of such models in accurately interpreting exoplanetary atmospheres. Under these temperature, irradiation, and transport conditions, non-equilibrium chemistry dominates over equilibrium chemistry. This necessity is further reinforced by the recent detection of SO_2 , a photochemical product, in the atmosphere of WASP-39 b (Rustamkulov et al. 2023; Alderson et al. 2023; Tsai et al. 2023). Non-equilibrium chemistry models applied to K2-18 b have also led to a reassessment of the retrieved abundances of CH_4 and CO_2 , favoring a higher CH_4 content and a lower CO_2 content (Wogan et al. 2024). Additionally, a reanalysis of JWST data reduction has cast doubt on the initial CO_2 detection itself (Schmidt et al. 2025), aligning with the findings from non-equilibrium chemistry models. This highlights the importance of accounting for non-equilibrium processes in atmospheric models and applying diverse data analysis techniques to ensure robust results, as emphasized by Schmidt et al. (2025).

Furthermore, the relatively low resolution of space-based observations compared to ground-based ones limits detection to only the major atmospheric constituents, making it difficult to detect minor gases. Chemical models are essential for inferring full atmospheric composition. However, such models still require observational constraints, particularly on metallicity and the C/O ratio. Previous studies using disequilibrium models have mainly explored metallicity, spanning a range from 1 to 1000 times the solar value (Charnay et al. 2021; Blain et al. 2021; Bézard et al. 2022). Analyses based on HST data (Tsiaras et al. 2019; Benneke et al. 2019) estimated metallicity between 100 and 300 times solar, consistent with Fortney et al. (2013), who predicted metallicity of approximately 100 to 400+ times solar for planets with radii of ~ 2 –4 Earth radii. Additionally, Bézard et al. (2022) explored eddy diffusion coefficients (K_{zz}) ranging from 10^5 to 10^{10} $\text{cm}^2.\text{s}^{-1}$, finding the best fit at 10^8 $\text{cm}^2.\text{s}^{-1}$. The C/O ratio is often assumed to be solar, as in Wogan et al. (2024), though Blain et al. (2021) proposed exploring a small range from 0.0013 to 2.2, with results favoring moderate C/O ratios. More recently, Schmidt et al. (2025) reanalyzed JWST data and investigated disequilibrium models with a metallicity of 100 times solar, K_{zz} of 10^7 $\text{cm}^2.\text{s}^{-1}$, and a C/O ratio ranging from solar to 4. They suggested that a high C/O ratio (≥ 3) may explain the non-detection of H_2O .

In this study, we aim to comprehensively explore the three key parameters simultaneously (metallicity, C/O ratio, and K_{zz}) using the non-equilibrium chemical model *FRECKLL* (Al-

Refaie et al. 2024) together with JWST observational data from Madhusudhan et al. (2023). Our goal is to better constrain these parameters and investigate the chemistry of minor species in K2-18 b, a temperate sub-Neptune located in the habitable zone of its host star.

2. Methods

Our method consists of three steps: running non-equilibrium chemical models across a three-dimensional parameter space (metallicity, C/O ratio, and K_{zz}), computing the corresponding theoretical spectra, and comparing these spectra to the observational data.

2.1. Observational data

We used the K2-18 b observational data from Madhusudhan et al. (2023). The spectrum was obtained from a single transit observation with each of JWST’s NIRISS SOSS and NIRSpec G395H instruments, covering a discontinuous wavelength range from 0.9 to 5.2 μm . As retrieved by Madhusudhan et al. (2023), the spectra exhibit an offset of -41 ppm between the NIRISS and NIRSpec data. For model comparison, we use the spectra at their native resolution and apply the χ^2 method. However, for visualization purposes, we present the lower-resolution spectra from Madhusudhan et al. (2023).

2.2. Equilibrium chemistry retrieval

Even though temperature, irradiation, and transport conditions indicate that non-equilibrium chemistry dominates over equilibrium chemistry, we performed a Bayesian retrieval assuming chemical equilibrium. The objective was to assess whether the current data can distinguish between equilibrium and non-equilibrium chemical states. For this purpose, we used *TauREx 3* (Tau Retrieval for Exoplanets)¹, a fully Bayesian inverse atmospheric retrieval framework (Al-Refaie et al. 2021).

TauREx 3 comprises two main components: the Forward Model framework and the Retrieval framework. The Retrieval framework aims to fit a forward model to observational data. As our equilibrium chemical model, we employed *ACE* (coupled with *TauREx 3*) (Agúndez et al. 2012, 2020), which has been identified by Jaziri et al. (2024) as the most suitable equilibrium chemistry model for our case.

We used absorption cross-sections computed by ExoMol (Yurchenko et al. 2011; Tennyson & Yurchenko 2012; Barton et al. 2013; Yurchenko et al. 2014; Barton et al. 2014), specifically those from Chubb et al. (2021), for the following species: H_2O , CO , CH_4 , CO_2 , H_2CO , HCN , C_2H_2 , NH_3 , and C_2H_4 . The temperature profile was fixed to match that used in the non-equilibrium chemical models. All free parameters and priors are shown in Table 1

After obtaining the best-fit model with *TauREx 3*, we calculated its χ^2 value, using the same procedure as for the non-equilibrium models, in order to directly compare the two approaches and evaluate whether the available data significantly favor non-equilibrium chemistry over equilibrium chemistry.

2.3. Non-equilibrium chemical model

To fit the observed spectrum and determine the chemical composition of the atmosphere of K2-18 b, we use the 1D non-

¹ <https://github.com/ucl-exoplanets/taurex3>

Table 1: Free parameters and priors for the retrieval with equilibrium chemistry.

Parameters	Bounds
$\log_{10}(P_{clouds})$ [Pa]	-2 to 6
radius [R_{jup}]	0.1 to 0.3
Chemistry	
\log_{10} [Metallicity]	-1 to 3
C/O	0.01 to 10

equilibrium chemical model *FRECKLL* (Al-Refaie et al. 2024). *FRECKLL* solves the steady-state continuity equations for each species, accounting for chemical production and loss as well as vertical transport via eddy diffusion. The chemical network includes ~ 2000 reactions (thermal and photochemical) among over 100 neutral species, involving the elements H, C, N and O. The reaction network is primarily adapted from the Venot et al. (2012) and Moses et al. (2011) frameworks, with updates to reaction rates and species relevant to temperate sub-Neptunes. We used specifically the Venot et al. (2020) chemical network, which is limited to well-characterized species containing up to two carbon atoms (C2). *FRECKLL* includes vertical mixing parameterized by a user-defined eddy diffusion coefficient (K_{zz}), and photolysis rates are computed using a two-stream approximation with stellar UV flux inputs. The model does not currently account for condensation processes, including H₂O cloud formation, which may impact the abundance profiles of condensable species at lower temperatures. Since this could impact the retrieved C/O ratio, we performed a parallel fit to the observations excluding the H₂O opacity, which biases the C/O ratio in the opposite direction.

FRECKLL has been originally designed to model equilibrium and disequilibrium chemistry on warm to hot hydrogen-dominated exoplanetary atmosphere (Venot et al. 2012, 2015, 2020; Veillet et al. 2024). However, it can also be applied to temperate atmospheres, with validation for temperatures ranging from 300 to 2500 K. We simulate the atmosphere of K2-18 b for a range of C/O ratio (from 0.1 to 100), metallicity (from 0.1 to 1000) and constant eddy diffusion coefficient (K_{zz} from 10^5 to 10^{10} cm².s⁻¹), see Table 2 for the grid range and resolution. To achieve a given C/O ratio, we adopt the approach of adjusting both carbon and oxygen abundances while conserving the overall metallicity.

Table 2: Non-equilibrium chemical model running grid.

Parameters	range	step	Npoint
\log_{10} [Metallicity]	[-1:3]	0.137	30
C/O	[0.1:10]	0.341	30
C/O	[10:20]	0.5	20
C/O	[20:100]	10	8
$\log_{10}[K_{zz}]$	[5:10]	1.0	6

Notes. The range, the number of points and the corresponding step are described. C/O have a higher resolution at lower values to better characterize the main variations and the lower limit. Total number of simulation are 30x58x6.

We used the temperature profile from Blain et al. (2021), corresponding to the best fit (metallicity = 175, C/O = 0.13,

$K_{zz} = 10^6$). We neglect, at first-order, temperature variations due to composition, as we do not expect significant changes in the overall trend. This is consistent with the findings of Blain et al. (2021), where the impact was shown to be small. The parameters of K2-18 b are listed in Table 3. For photochemistry, we used MUSCLES GJ 436 version 2.2 stellar spectra (France et al. 2016; Youngblood et al. 2016; Loyd et al. 2016) as a proxy for K2-18, as suggested by dos Santos et al. (2020).

Table 3: Planet-Stellar K2-18 b parameters.

Parameters	Values
R_* [Rsun]	0.4445
T_* [K]	3457
R_p [Rjup]	0.2328
a [AU]	0.1591
g [m/s ²]	12 (at 100bar)
Reference	Benneke et al. (2019)

Notes. Used for *FRECKLL* and *TauREx* simulations.

2.4. Fitting to observation

With the atmospheric profiles output by *FRECKLL*, we used the Forward Model framework of *TauREx 3* (Al-Refaie et al. 2021) to generate transmission spectra. We considered the same cross-sections and molecules as for the equilibrium chemistry retrieval.

We adjusted the theoretical spectra to match the K2-18 b observational *native resolution* data from Madhusudhan et al. (2023) by retrieving the planet’s radius. Then, we computed the chi-square (χ^2) to determine the best-fit models. As in Blain et al. (2021) and Wogan et al. (2024), this approach provides an initial insight into the most accurate non-equilibrium chemical model compared to observations, though it has not yet been fully implemented within retrieval model frameworks. We estimate a good fit at 2σ .

We reduce the 3D parameter space (metallicity, C/O, K_{zz}) to 2D by selecting the minimum χ^2 values along the K_{zz} dimension, in order to explore the effects of metallicity and C/O. The best-fit model corresponds to the minimum χ^2 , with 1σ , 2σ , 3σ , and 4σ uncertainties in a 2D parameter space, defined as a $\Delta\chi^2$ difference from the best fit, with values of 2.30, 6.18, 11.83, and 19.33, respectively. To refine our estimates, we fit (polynomial fit) the projected $\Delta\chi^2$ over the C/O ratio and metallicity, obtaining the best-fit values along with 1σ , 2σ and 3σ confidence intervals. The projected $\Delta\chi^2$ is obtained by reducing the 2D parameter space to 1D, selecting the models with the lowest χ^2 values along the collapsed dimension. In a 1D parameter space 1σ , 2σ , 3σ , 4σ , and 5σ uncertainties correspond to values of 1, 4, 9, 16, and 25, respectively.

This method provides an estimate of the C/O ratio and metallicity of K2-18 b, which in turn constrains the abundances of minor species. Additionally, we fitted a flat-line model to the observed spectrum and we calculated the associated χ^2 to assess the significance of our retrieved models, ensuring that they provide a better fit than scenarios such as a bare rock with no atmosphere or a gas giant with a cloud layer.

3. Results

Table 4 summarizes the key results for non-equilibrium chemical models. Metallicity, C/O ratio, and K_{zz} were calculated using a polynomial fit to the global trend. Best-fit abundances and their 3σ uncertainties were derived from the explored model grid. The best-fit values (on the model grid) are 280.7 for metallicity, 90.0 for the C/O ratio, and $10^6 \text{ cm}^2 \text{ s}^{-1}$ for K_{zz} , with a corresponding χ^2 of 4786.25.

Table 4: Retrieved parameters and species abundances of the best fit.

Parameters	Values
Metallicity (1σ)	266^{+90}_{-61}
Metallicity (2σ)	266^{+291}_{-104}
Metallicity (3σ)	≥ 129
C/O (1σ)	≥ 7.1
C/O (2σ)	≥ 2.1
C/O (3σ)	≥ 0.96
$K_{zz} [\text{cm}^2 \cdot \text{s}^{-1}]$	All within 1σ
Abundances at 1 mbar of best fit at 3σ	
$\log_{10}[\text{CH}_4]$	$-0.3^{+0.1}_{-1.7}$
$\log_{10}[\text{CO}_2]$	$-5.6^{+4.9}_{-0.9}$
$\log_{10}[\text{CO}]$	$-2.2^{+1.8}_{-0.6}$
$\log_{10}[\text{H}_2\text{O}]$	$-4.2^{+3.5}_{-4.3}$
$\log_{10}[\text{NH}_3]$	$-3.8^{+0.6}_{-5.8}$
$\log_{10}[\text{H}_2\text{CO}]$	$-12.6^{+5.9}_{-1.1}$
$\log_{10}[\text{CH}_3\text{OH}]$	$-9.6^{+3.3}_{-4.0}$
$\log_{10}[\text{CH}_3\text{CHO}]$	$-11.3^{+4.0}_{-1.8}$
$\log_{10}[\text{C}_2\text{H}_2]$	$-7.0^{+4.0}_{-7.5}$
$\log_{10}[\text{C}_2\text{H}_4]$	$-9.6^{+8.6}_{-1.1}$
$\log_{10}[\text{C}_2\text{H}_6]$	$-4.1^{+2.2}_{-2.0}$
$\log_{10}[\text{N}_2]$	$-1.4^{+0.3}_{-0.5}$

Notes. It is calculated using *FRECKLL* and *TauREx* simulations compared to JWST data (Madhusudhan et al. 2023). The species abundances values are taken at 1 mbar, which is representative to the probed atmosphere.

3.1. Transmission spectra

The transmission spectra within 3σ of the best fit are shown in Figure 1, with the shaded area representing the uncertainty. The main spectral features are attributed to CH_4 , CO_2 , and CO , while secondary features from H_2O and NH_3 can be observed near 2 and $3 \mu\text{m}$ (see Figure 2).

The significance of the disequilibrium models was assessed by comparing them to a flat-line retrieval (see Figure 1). The χ^2 calculations (Figure 4) indicate that the best disequilibrium model achieves a confidence level exceeding 4σ compared to the flat-line model. This confirms the robustness of the observed spectral features and the validity of the best disequilibrium model.

3.2. Equilibrium chemistry retrieval

The best fit is found for a metallicity of 71^{+58}_{-20} and a C/O ratio of $6.78^{+5.8}_{-2.0}$ (see Figure A.1 in Appendix A). The spectral features are primarily attributed to CH_4 and CO_2 (see Figure A.2 in Appendix A). We observe little difference between equilibrium and non-equilibrium chemistry for the only strongly detected species, CH_4 (see Figures A.3 in Appendix A and 3). In fact, the calculated χ^2 of the best-fit equilibrium chemical model is slightly lower than that of the best non-equilibrium model ($\Delta\chi^2 = -2.0$, so within 1σ of the 2D space), indicating a marginally better fit with equilibrium chemistry, even though we know that the atmosphere is expected to be in a non-equilibrium chemical state.

Nevertheless, non-equilibrium chemistry significantly affects the abundances of H_2O , NH_3 , and CO_2 , which can either increase or decrease depending on metallicity and the C/O ratio. However, these variations remain below current detection limits.

3.3. Eddy diffusion coefficient

The K_{zz} is not constrained by our analysis. When reducing the 3D parameter space to 1D by selecting models with the lowest χ^2 values across the metallicity and C/O dimensions, the resulting χ^2 values remain within 1σ of the best fit. Near the best-fit metallicity, variations in K_{zz} result in χ^2 fluctuations of less than 1σ .

Figure 3 shows the species profiles of the best-fit model. The shaded area represents the dispersion in K_{zz} . This illustrates that while vertical transport significantly affects minor species, it has little impact on major species, particularly CH_4 . This explains why K_{zz} remains unconstrained in our analysis.

Figure 4 presents the evolution of $\Delta\chi^2$ as a function of metallicity and C/O. Each parameter is projected along the other dimension using the lowest χ^2 values. The shaded regions represent the dispersion due to variations in K_{zz} over its entire range (from 10^5 to $10^{10} \text{ cm}^2 \cdot \text{s}^{-1}$). The general trend is represented by the median value, which is used to determine the best-fit values or lower limits for metallicity and C/O through polynomial fitting, as shown in Figure 4. The corresponding numerical values are reported in Table 4.

3.4. Metallicity

Metallicities $\lesssim 100$ are statistically less significant than a flat line, as shown in Figure 4. The best fit found in our model grid corresponds to a metallicity of 280.7. Using a polynomial fit, we derived a 2σ confidence interval of 266^{+291}_{-104} , as shown in Figure 4 and reported in Table 4. Within our modeled grid, we could only establish a 3σ lower limit of ≥ 129 . Figure 5, which presents $\Delta\chi^2$ as a function of metallicity and C/O, shows that this is primarily due to the large uncertainty in metallicity at low C/O values. An upper limit at 3σ might be obtained by extending the metallicity grid beyond 1000, though the benefit of doing so appears limited. Two distinct regimes can be identified:

C/O ratio $\lesssim 2$ High metallicity are favored ($\gtrsim 100$). But, the metallicity has huge uncertainties between 100 and 1000.

C/O ratio $\gtrsim 2$ Increasing the C/O ratio constrains the metallicity between 205 and 356 at 1σ of the best fit (see Figure 4). This follows Fortney et al. (2013) expectation considering the radius

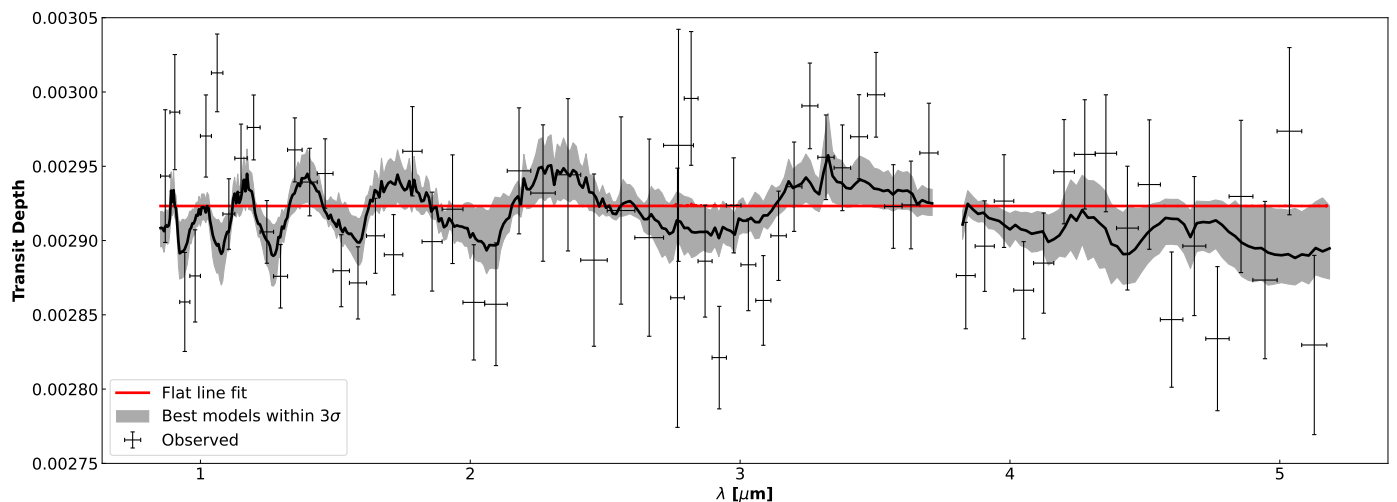


Fig. 1: Transit spectra of non-equilibrium 1D models at resolution 200, compare to K2-18 b observation (Madhusudhan et al. 2023) low resolution representation with an offset of -41 ppm between NIRISS and NIRSPEC data. Solid Gray line is the median value of the 3σ dispersion from the best fit represented with the shaded area. Red line is the best flat line retrieval.

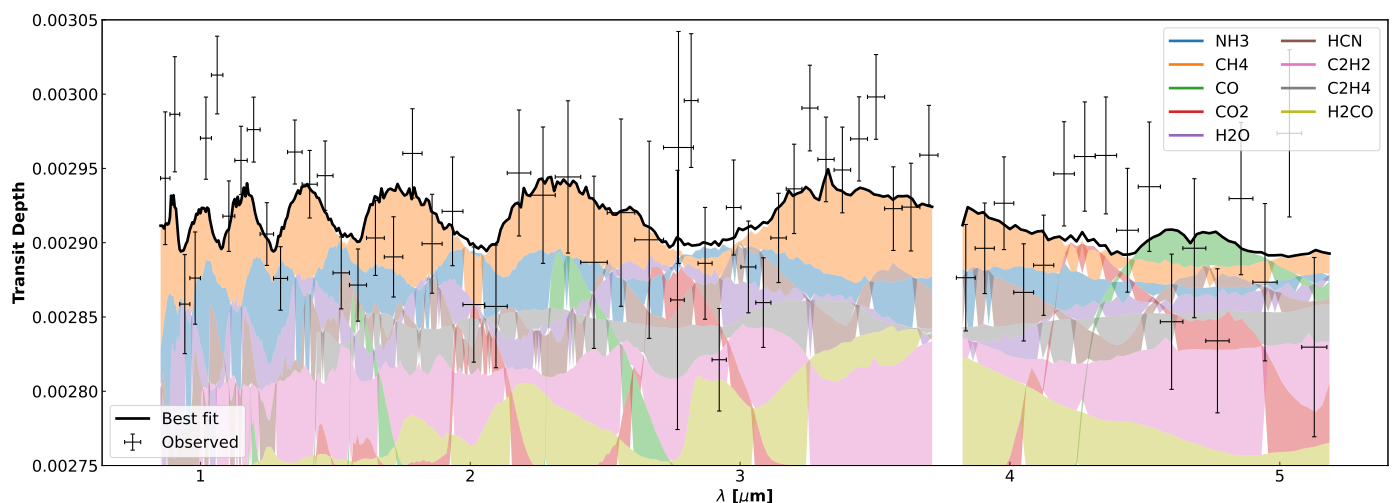


Fig. 2: Transit spectra of the best fit non-equilibrium 1D model at resolution 200 (black solid line). This is the approximate best fit on the simulated grid of metallicity, C/O and K_{zz} . Values are respectively 280.7, 90.0 and 10^6 $\text{cm}^2 \cdot \text{s}^{-1}$. It is compared to K2-18 b observation (Madhusudhan et al. 2023) low resolution representation with an offset of -41 ppm between NIRISS and NIRSPEC data. The contributions of considered molecules are represented with shaded colors.

of the planet.

Figure 5 is zoomed for $C/O \leq 10$ since until 100 it follows the same trend.

3.5. C/O ratio

Low C/O ratio, close to solar C/O ($0.55^{+0.130}_{-0.108}$ Lodders (2019)), are statistically as significant as a flat line, as shown in Figure 4. Our results favor a high C/O ratio (see Figure 5). We are only able to constrain a lower limit on the C/O ratio: values above 7.1 lie within 1σ of the best fit, while the solar C/O ratio is ruled out at 3σ confidence level (see Figure 4 and Table 4). Excluding H_2O opacity slightly changes the retrieved C/O ratio. The most affected values are at the 2σ and 3σ confidence levels, which decrease to 1.4 and 0.57, respectively, compared to the original

values of 2.1 and 0.96. Accounting for H_2O condensation would yield values that lie in between.

3.6. Abundances

Figure 6 shows the profiles of key species within the 3σ uncertainty range. The abundances at 1 mbar for the best-fit model, along with their 3σ uncertainties, are also shown in Figure 6 and reported in Table 4. This pressure level corresponds to the region probed by the observations, where the abundance profiles are shown also to be relatively vertically constant in the model.

At 3σ , CH_4 , CO_2 , CO , H_2O , and C_2H_4 can reach mixing ratios of up to 10% (see Figure 6). However, CO_2 , H_2O , and C_2H_4 can also fall below the ppm level, meaning we cannot confidently claim a detection for these species. In contrast, CH_4 is well constrained, with an abundance consistently above 1%.

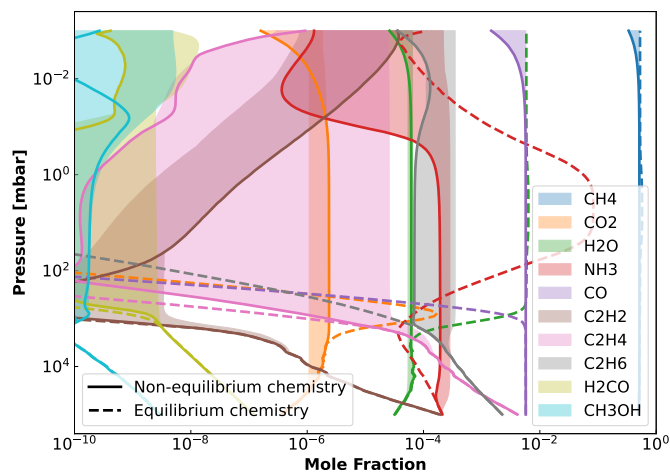


Fig. 3: Species profiles of the best fit of non-equilibrium 1D models (solid lines) and of equivalent equilibrium chemistry model (dash lines). This is the best fit on the models grid with metallicity of 280.7, C/O of 90.0, and K_{zz} of $10^6 \text{ cm}^2 \cdot \text{s}^{-1}$. The shaded area represent the dispersion of K_{zz} from 10^6 to $10^{10} \text{ cm}^2 \cdot \text{s}^{-1}$.

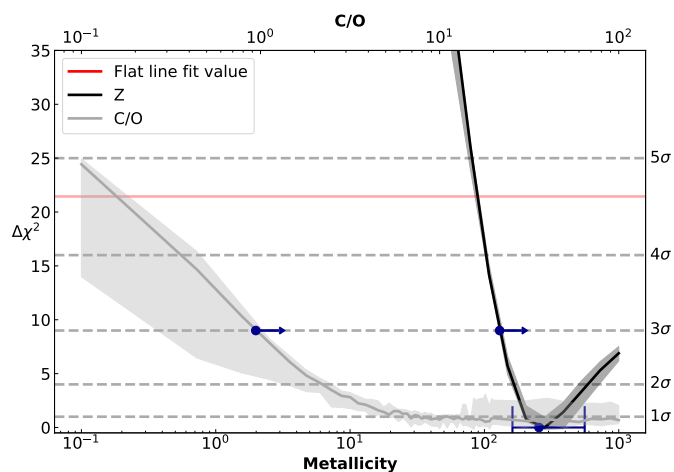


Fig. 4: Evolution of $\Delta\chi^2$ with metallicity or C/O ratio. The χ^2 values are computed by comparing 1D chemical models to the K2-18 b observations from Madhusudhan et al. (2023). The $\Delta\chi^2$ values represent the difference from the best-fit model. The 1D projection is obtained by selecting the lowest χ^2 across the other parameter dimension (metallicity or C/O). The shaded area represent the dispersion from K_{zz} that have no preferred value (within 1σ), while the solid line indicates the median across K_{zz} values. The red line represents the $\Delta\chi^2$ for the best flat-line retrieval, demonstrating a confidence level of the best fit exceeding 4σ . An additional best fit value with a 2σ uncertainty for metallicity and a lower limit at 3σ for metallicity and C/O are shown in blue, derived from a polynomial fit in log scale.

Additionally, oxidized species such as H_2CO , CH_3OH , and CH_3CHO can reach mixing ratios close to the ppm level (see Figure 6). While CH_4 remains the only strongly confirmed detection, a variety of chemically interesting species may be present in significant amounts.

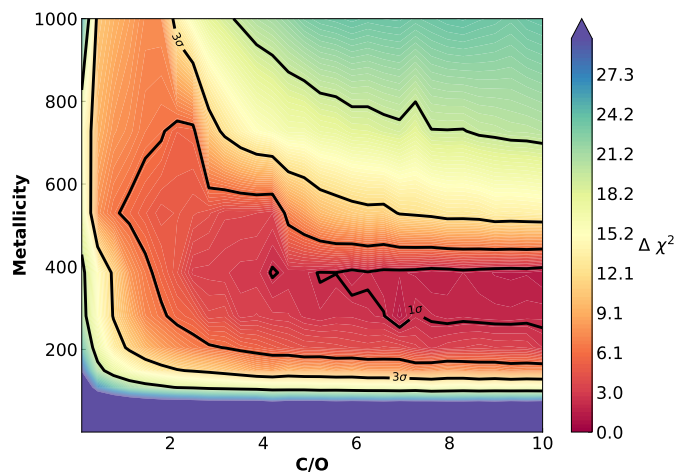


Fig. 5: Representation of the $\Delta\chi^2$ with the best fit compared to K2-18 b observation (Madhusudhan et al. 2023) and the 1D models. The 2D map goes over the range of metallicity and C/O ratio, collapsed in K_{zz} with best χ^2 . The 2D map is zoomed for C/O ratio ≤ 10 since above it follows the same trend.

4. Discussion

4.1. Species detection

To accurately characterize the atmosphere of K2-18 b, particularly under its specific temperature, irradiation, and vertical transport conditions, it is essential to use comprehensive chemical models that incorporate non-equilibrium processes. The motivation for using such models arises not only from their better agreement with retrieved atmospheric abundances but also from the limitations imposed by the low signal-to-noise ratio (SNR) of current observations, which limits our ability to constrain the full atmospheric composition. While the atmosphere of K2-18 b is likely chemically rich, retrievals assuming constant abundance profiles can confidently confirm only the presence of CH_4 .

The CH_4 and CO_2 detections with inferred abundances of $\sim 1\%$ reported by Madhusudhan et al. (2023) are within 3σ of our best-fit model. However, as shown in Figure 6, CH_4 appears more abundant than CO_2 , an observation consistent with disequilibrium models such as those by Wogan et al. (2024). Moreover, our analysis shows that CO_2 abundances can drop as low as $\log_{10}[\text{CO}_2] = -6.5$ at 1 mbar (Table 4), aligning with the findings of the reanalysis by Schmidt et al. (2025). The large uncertainty in CO_2 abundance retrieved with non-equilibrium models further supports the conclusion of Schmidt et al. (2025), who, unlike Madhusudhan et al. (2023), question the robustness of the CO_2 detection.

Indeed, the updated data reduction from Schmidt et al. (2025) limits the confirmed detections to CH_4 , casting further doubt on the presence of CO_2 . This is evident from the increased uncertainty around the $4.2 \mu\text{m}$ CO_2 band and the wide range of retrieved abundances in our analysis (see Figure 6). Nevertheless, this does not rule out the presence of CO_2 or other minor species. As shown in Figure 2, several of these compounds may still contribute to the observed spectrum and could exist in significant quantities, albeit below current detection thresholds.

Other species such as CO , H_2O , and C_2H_4 can reach mixing ratios of a few percent but remain undetected, likely because their spectral signatures are either masked by CH_4 or buried in observational noise. Our results, for instance, indicate substantial CO abundances (Figure 6 and Table 4) with a notable spec-

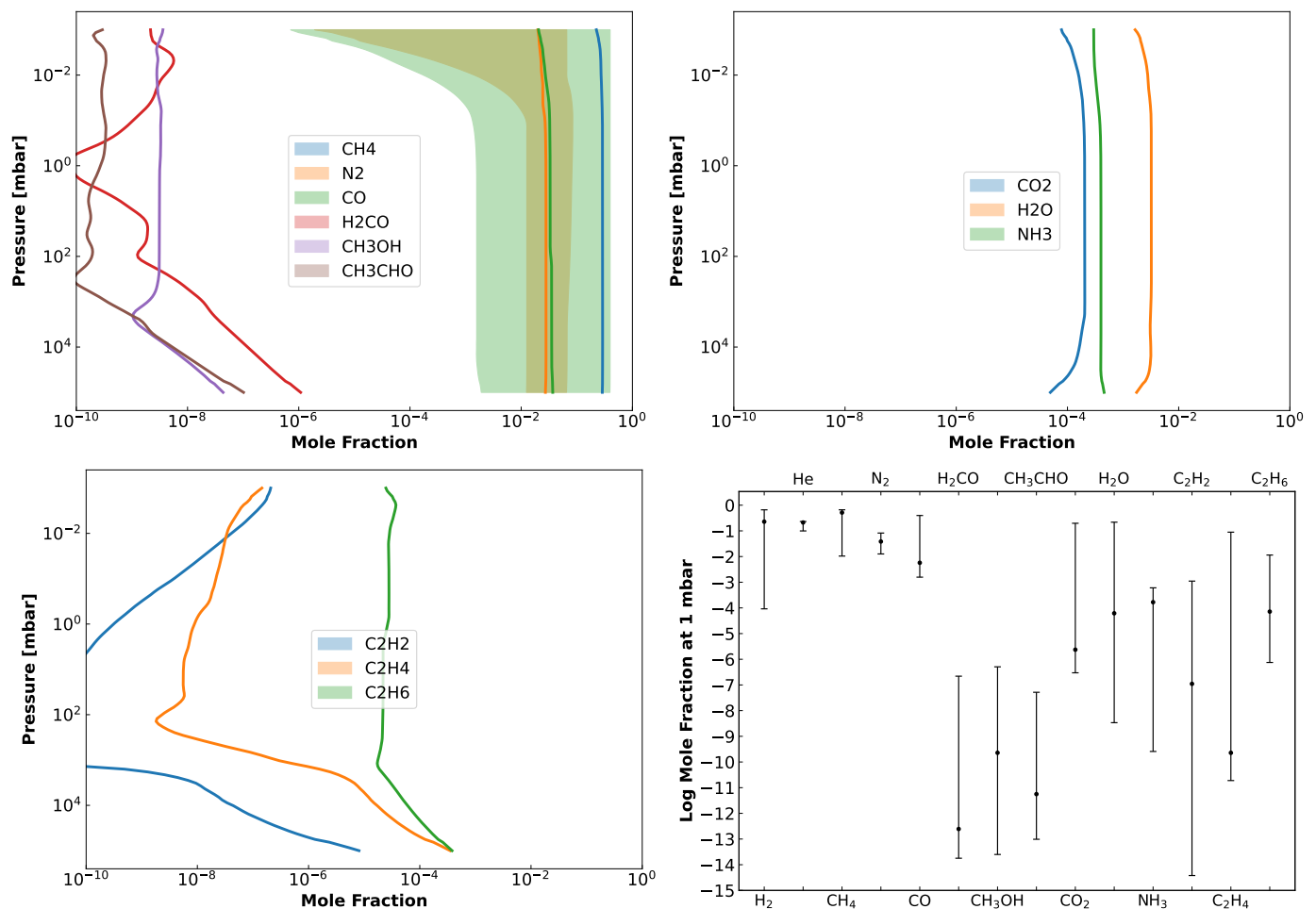


Fig. 6: Species profiles of non-equilibrium 1D models within 3σ of the best fit, compare to K2-18 b observation (Madhusudhan et al. 2023). Solid line is the median value of the dispersion represented with the shaded area. Bottom right shows values at 1 mbar with a dot for the best fit model on the parameter space grid.

tral feature near $5\ \mu\text{m}$ (Figure 2), despite CO not being detected in previous studies. This non-detection likely stems from large data uncertainties affecting CO’s spectral features, an issue that similarly impacts other secondary species like H_2O and NH_3 .

NH_3 , in particular, can reach $\log_{10}[\text{NH}_3] = -3.2$ at 1 mbar (Table 4), consistent with predictions from disequilibrium models such as Wogan et al. (2024), and contributes to secondary features in the spectrum (Figure 2). Unlike Madhusudhan et al. (2023) and Schmidt et al. (2025), who reported upper limits of $\log_{10}[\text{NH}_3] = -4.51$ and -5.25 respectively, our disequilibrium model accommodates higher NH_3 abundances without requiring nitrogen depletion, challenging the interpretation by Schmidt et al. (2025). The apparent absence of NH_3 in the spectra is more consistent with a gas mini-Neptune scenario rather than the purely Hycean interpretation proposed by Madhusudhan et al. (2023). It is important to note, however, that nitrogen may be sequestered through dissolution in deep magma oceans, as proposed by Shorttle et al. (2024), thereby lowering its atmospheric abundance. Consequently, the upper bound of $\log_{10}[\text{NH}_3] \lesssim -3.2$ should not be interpreted as a strict observational constraint but rather as a model-limited outcome under the assumption of undepleted nitrogen. Additionally, since our approach assumes a fixed P–T profile, the retrieved abundance of NH_3 is subject to uncertainty, and should be interpreted as indicative of chemical trends rather than precise values.

Similarly, the atmospheric H_2O abundance predicted by our models may be biased high, since *FRECKLL* does not include condensation processes. In K2-18 b’s cool upper atmosphere, H_2O vapor could condense and rain out, effectively reducing the gas-phase abundance in the observable layers. Despite these biases favoring higher-than-realistic abundances of NH_3 and H_2O , neither species is robustly detected in the current data. Their spectral features appear to be masked by dominant absorbers such as CH_4 or buried in observational noise. This suggests that even if these molecules were present at relatively high levels, current observations lack the sensitivity and spectral resolution to confirm their presence.

As also seen in Figure 6, although the amplitude of spectral features in the best-fit models may appear smaller than in the observed data, these differences remain within the observational uncertainties. A key source of this mismatch is the lack of accurate model fitting at shorter wavelengths ($\leq 2\ \mu\text{m}$), where a decreasing trend, likely caused by aerosols, is not captured. This limitation leads to challenges in simultaneously fitting the $1\text{--}2\ \mu\text{m}$ and $2\text{--}5\ \mu\text{m}$ spectral ranges. As a result, models with pronounced features may overfit one region while underfitting the other. This discrepancy could also affect the retrieved C/O ratio, as the CO and CO_2 bands can be sensitive to the global shift and may be misrepresented without proper aerosol modeling.

A major challenge in atmospheric retrieval is that dominant spectral features, especially those of CH_4 , can obscure the signatures of other potentially abundant species such as H_2O and NH_3 (see Figure 2). To resolve these overlapping signals, high-resolution ground-based spectroscopy offers a promising approach. Such observations could enable the detection of minor species, such as H_2CO , CH_3OH , and CH_3CHO , which may exist at ppm levels (see Figure 6 and Table 4). While K2-18 b remains a challenging target, upcoming instruments on next-generation telescopes, such as ANDES on the ELT, are expected to achieve the SNR necessary to detect hidden species like H_2O and NH_3 (Palle et al. 2025), helping refine our understanding of K2-18 b's chemical inventory.

4.2. Bimodality of the metallicity

In contrast to the uncertainties surrounding other parameters, all analyses consistently support a high atmospheric metallicity for K2-18 b, exceeding 100 times the solar value. However, when the C/O ratio is assumed to be near the solar value, metallicities up to nearly 1000 still fall within the 1σ confidence interval. This trend was already observed in HST data by Bézard et al. (2022), which underlines the fact that the entire spectrum is dominated by CH_4 absorption bands, consistent with CH_4 being the only species robustly detected. This uncertainty aligns with the observation that, at low C/O ratios, the $\Delta\chi^2$ values become comparable to that of a flat line (see Figure 4), indicating that high-metallicity models, which naturally produce flatter spectra, can still yield statistically acceptable fits.

The implications of such high metallicity have been tempered in previous studies by invoking the formation of clouds, which become more likely at elevated metallicities due to the increased partial pressure of H_2O . These clouds can further flatten the spectrum, as discussed in Charnay et al. (2021) and Blain et al. (2021). However, these interpretations did not account for the potential effects of elevated C/O ratios.

In this study, by modeling an extensive grid spanning both metallicity and C/O ratio, we place tighter constraints on the atmospheric metallicity. Our results indicate that the metallicity is likely between 162 and 557 at the 2σ level (Table 4). Metallicities above ~ 500 become inconsistent with the data when paired with high C/O ratios (in contrast to low C/O ratios ≤ 2). This is because, while high metallicity flattens the spectrum, it also leads to C_2H_4 dominating over CH_4 , resulting in a poorer match to the observed features.

The observed bimodality in the metallicity distribution, between low and high C/O regimes, emerges only because we explore the full joint parameter space of metallicity and C/O ratio. Studies assuming a fixed solar C/O ratio, as done in previous work (Charnay et al. 2021; Bézard et al. 2022; Wogan et al. 2024), exclude only low metallicities (i.e., ≤ 100). By extending the exploration to elevated C/O ratios for the first time, we are able to observe this bimodality and place significantly stronger constraints on the metallicity of K2-18 b.

4.3. A high C/O ratio

Madhusudhan et al. (2023) predict a low C/O ratio, based on the detection of both CO_2 and CH_4 at $\sim 1\%$. This interpretation is used to favor a Hycean world over a deep atmosphere scenario, given the absence of detectable NH_3 and CO features, which should be present in significant quantities in a deep atmosphere with a low C/O ratio. However, the free retrieval approach em-

ployed in their study relies primarily on the dominant spectral features to estimate the C/O ratio. In contrast, our results show that NH_3 and CO can exist in substantial amounts without being detected, due to the high noise and large uncertainties in the data, especially when exploring scenarios with higher C/O ratios (see Figure 2). Such high C/O ratio scenarios have not been explored in previous studies, whereas our analysis favors a high C/O ratio (see Figure 5), consistent with the conclusions of Schmidt et al. (2025).

While Schmidt et al. (2025) suggested a high C/O (≥ 3) based on the 2σ uncertainty in the retrieved H_2O abundance ($\log_{10}[\text{H}_2\text{O}] < -3.05$), our analysis is based on the full spectral contributions. Nonetheless, our results are consistent within the 1σ to 2σ lower limits reported in Table 4. However, as our approach assumes a fixed P-T profile, the derived constraints on the C/O ratio carry additional uncertainties, and should be viewed as indicative of chemical trends rather than precise determinations. Additionally, we demonstrated that the absence of H_2O condensation in the model introduces a bias. The retrieved C/O ratio should give slightly reduce value, but not by more than 1.4 (at 2σ).

This unusually explored and finding of a high C/O ratio in an H_2 -dominated atmosphere is therefore consistent with the observed CH_4 -rich spectrum. A carbon-rich atmosphere would naturally enhance aerosol formation, which may contribute to the spectral slope observed at wavelengths $\leq 2\mu\text{m}$ (Madhusudhan et al. 2023), a feature not captured by our models. However, current constraints on aerosols remain limited (Madhusudhan et al. 2023; Schmidt et al. 2025).

The C/O ratio cannot be reliably constrained using free retrieval methods alone and instead requires comprehensive disequilibrium chemical models for accurate inference. Even with such models, our results show that the C/O ratio is only constrained with a lower limit. This limitation stems from the current observational data, which do not provide strong constraints on species particularly sensitive to the C/O ratio. Consequently, this calls into question the reliability of using the C/O ratio alone to infer atmospheric chemistry. As noted by Turrini et al. (2021), breaking the degeneracy in the C/O ratio, especially for giant planets, may require additional elemental ratios such as C/N, N/O or even S/N. Kama et al. (2019) and Kama et al. (2025) also suggested S/H, S/O and P/H ratio. However, in our case, there are no strong constraints on nitrogen-bearing species, limiting our ability to derive meaningful estimates of the C/N or N/O ratios, and the chemical network does not contain any S and P species.

At present, no single elemental ratio reliably constrains disequilibrium models, and, by extension, the overall atmospheric composition, without better constraints on additional species beyond CH_4 . As shown in Figure 2, both CO_2 and CO exhibit strong spectral features between 4 and $5\mu\text{m}$, but these features are poorly constrained due to the low SNR in this wavelength range. Since the abundances of CO and CO_2 are critical for constraining the C/O ratio, further transit observations with NIR-Spec G395H would be particularly valuable for resolving this issue and advancing our understanding of the atmospheric composition of K2-18 b.

4.4. Unconstrained vertical mixing in the atmosphere

The variation of the eddy diffusion coefficient (K_{zz}) has no significant impact on the model fits and remains within the 1σ uncertainty range across the best-fit solutions within the 3σ confidence interval for metallicity. Similar conclusions were drawn

by Blain et al. (2021) and Bézard et al. (2022). This insensitivity is primarily due to the lack of observational constraints on species that are strongly influenced by variation of vertical quenching, which is governed by the transport efficiency parameterized by K_{zz} . In particular, the CH_4 abundance profile remains nearly constant and shows little dependence on K_{zz} within the explored metallicity range and pressure levels (see Figures 6 and 3). Thus, although vertical transport causes notable deviations from chemical equilibrium, variations in K_{zz} themselves do not significantly constrain the data; rather, they introduce additional uncertainty in the retrieved abundances of minor species.

4.5. What can we really learn from the observational data?

Finally, many strong conclusions remain limited due to the large uncertainties in the observational data. Even when using self-consistent models with non-equilibrium chemistry, we are constrained by the lack of sufficient data precision. Given that only one molecule, CH_4 , is robustly detected, no meaningful upper limit on the C/O ratio can be determined. We further demonstrate, using a Bayesian retrieval with an equilibrium model, that the presence of non-equilibrium chemistry in the atmosphere of K2-18 b cannot be conclusively proven. In fact, the best-fit equilibrium model is statistically more significant than the non-equilibrium model, with a $\Delta\chi^2 = -2$.

Nevertheless, we can still confidently conclude the detection of CH_4 , a correspondingly high C/O ratio of ≥ 2.1 at the 2σ level, and a metallicity of 266_{-104}^{+291} at 2σ , acknowledging that these retrieved values are subject to model uncertainties due to the use of a fixed P–T profile.

5. Conclusion

In this study, we applied non-equilibrium chemical models to gain deeper insights into the atmosphere of K2-18 b, a temperate sub-Neptune located within the habitable zone of an M-dwarf star. By combining the latest observational data from the JWST with the *FRECKLL* chemical model, we explored the planet’s atmospheric composition and the underlying chemical processes in detail. Our analysis provides a comprehensive view of the key parameters (metallicity, C/O ratio, and K_{zz}) that shape the atmospheric composition of K2-18 b. We explored for the first time such high C/O ratio (from 0.1 to 100) showing the importance exploring simultaneously those 3 key parameters. We warn that accurately constraining the planet’s atmospheric composition requires more than traditional retrieval models assuming constant abundances; it also necessitates non-equilibrium models to address the limited species constraints imposed by the low SNR of the data.

Our results suggest a high atmospheric metallicity, exceeding 100 times the solar value. This finding aligns with previous studies, supports the planet’s potential for complex atmospheric chemistry, and constrains the metallicity to be below 558 at 2σ , acknowledging model uncertainties due to the use of a fixed P–T profile. We confirm that the presence of CH_4 is robustly detected, while the detection of CO_2 remains uncertain due to significant observational noise and large uncertainties. The abundances of minor species such as CO, H_2O , and NH_3 , although not directly detectable, are predicted to be present in notable quantities, suggesting the chemical diversity of the atmosphere. These findings underscore the importance of non-equilibrium models for accurately interpreting exoplanetary atmospheres, especially in the case of temperate sub-Neptunes, where disequilibrium processes likely play a significant role. Non-equilibrium models offer a

powerful tool to go beyond the limits of detectability, enabling us to investigate the hidden chemical processes and probe the plausible abundances of undetected species.

Our study also highlighted the challenges in constraining the C/O ratio with the available data. While we established a lower limit for the C/O ratio of 2.1 at the 2σ level, we cannot derive any specific value overall, pointing to the need for higher-quality data. However, the high C/O ratio and the apparent decreasing trend at lower wavelength $\leq 2\mu\text{m}$ can suggest the presence of hazes. The variation of eddy diffusion (K_{zz}) was found to have minimal impact on our results, consistent with previous studies, due to the lack of strong constraints from species influenced by variation of vertical mixing.

In conclusion, K2-18 b’s atmosphere is likely to be chemically rich and complex. Our work lays the foundation for future studies aimed at better understanding the atmospheric dynamics, chemistry, and potential habitability of temperate sub-Neptunes, which remain a promising class of exoplanets for future investigations into the possibility of life beyond our solar system.

In perspective, future observations with JWST’s NIRSpec G395H mode will significantly improve the SNR in the 4–5 μm range, enabling more precise constraints on CO and CO_2 , which exhibit strong spectral features in this wavelength region and are key tracers of the atmospheric C/O ratio. Complementarily, high-resolution spectroscopy with ELT/ANDES will provide unprecedented sensitivity and spectral resolution, facilitating the detection of spectrally blended or weak features from major species such as H_2O and NH_3 . These molecules are crucial not only for characterizing atmospheric composition but also for constraining elemental ratios such as C/O and N/H. Together, these next-generation facilities will give more robust constraints on atmospheric non-equilibrium chemistry. This synergy between space- and ground-based platforms will be essential for a more comprehensive characterization of temperate sub-Neptune atmospheres like that of K2-18 b.

Acknowledgements. This project has received funding from the European Research Council (ERC) under the ERC OxyPlanets projects (grant agreement No. 101053033). This project acknowledges funding from the European Research Council (ERC) under the European Union’s Horizon 2020 research and innovation programme (grant agreement No. 679030/WHIPLASH). O.V. acknowledges funding from the ANR through the project ‘EXACT’ (ANR-21-CE49-0008-01), as well as from the Centre National d’Études Spatiales (CNES). We would like to thank the anonymous referee for his pertinent comments, which improved the presentation of our results.

References

- Agúndez, M., Martínez, J. I., de Andres, P. L., Cernicharo, J., & Martín-Gago, J. A. 2020, *A&A*, 637, A59
- Agúndez, M., Venot, O., Iro, N., et al. 2012, *A&A*, 548, A73
- Al-Refaié, A. F., Changeat, Q., Waldmann, I. P., & Tinetti, G. 2021, *ApJ*, 917, 37
- Al-Refaié, A. F., Venot, O., Changeat, Q., & Edwards, B. 2024, *ApJ*, 967, 132
- Alderson, L., Wakeford, H. R., Alam, M. K., et al. 2023, *Nature*, 614, 664
- Barton, E. J., Chiu, C., Golpayegani, S., et al. 2014, *MNRAS*, 442, 1821
- Barton, E. J., Yurchenko, S. N., & Tennyson, J. 2013, *MNRAS*, 434, 1469
- Benneke, B., Werner, M., Petigura, E., et al. 2017, *ApJ*, 834, 187
- Benneke, B., Wong, I., Piaulet, C., et al. 2019, *ApJ*, 887, L14
- Blain, D., Charnay, B., & Bézard, B. 2021, *A&A*, 646, A15
- Bézard, B., Charnay, B., & Blain, D. 2022, *Nature Astronomy*, 6, 537
- Cabot, S. H. C., Madhusudhan, N., Constantinou, S., et al. 2024 [arXiv:2403.18891]
- Charnay, B., Blain, D., Bézard, B., et al. 2021, *A&A*, 646, A171
- Chubb, K. L., Rocchetto, M., Yurchenko, S. N., et al. 2021, *A&A*, 646, A21
- dos Santos, L. A., Ehrenreich, D., Bourrier, V., et al. 2020, *A&A*, 634, L4
- Fortney, J. J., Mordasini, C., Nettelmann, N., et al. 2013, *ApJ*, 775, 80
- France, K., Loyd, R. O. P., Youngblood, A., et al. 2016, *ApJ*, 820, 89

- Fressin, F., Torres, G., Charbonneau, D., et al. 2013, *The Astrophysical Journal*, 766, 81
- Gillon, M., Triaud, A. H. M. J., Demory, B.-O., et al. 2017, *Nature*, 542, 456
- Günther, M. N., Pozuelos, F. J., Dittmann, J. A., et al. 2019, *Nature Astronomy*, 3, 1099
- Hardegree-Ullman, K. K., Cushing, M. C., Muirhead, P. S., & Christiansen, J. L. 2019, *AJ*, 158, 75
- Jaziri, A. Y., Pluriel, W., Bocchieri, A., et al. 2024, *A&A*, 684, A25
- Kama, M., Shorttle, O., Borthakur, S. P. D., et al. 2025, arXiv e-prints, arXiv:2504.14228
- Kama, M., Shorttle, O., Jermyn, A. S., et al. 2019, *ApJ*, 885, 114
- Lodders, K. 2019, arXiv e-prints, arXiv:1912.00844
- Loyd, R. O. P., France, K., Youngblood, A., et al. 2016, *ApJ*, 824, 102
- Luger, R. & Barnes, R. 2015, *Astrobiology*, 15, 119
- Madhusudhan, N., Sarkar, S., Constantinou, S., et al. 2023, *ApJ*, 956, L13
- Moses, J. I., Visscher, C., Fortney, J. J., et al. 2011, *ApJ*, 737, 15
- Owen, J. E. & Mohanty, S. 2016, *MNRAS*, 459, 4088
- Palle, E., Biazzo, K., Bolmont, E., et al. 2025, *Experimental Astronomy*, 59, 29
- Ricker, G. R., Winn, J. N., Vanderspek, R., et al. 2015, *Journal of Astronomical Telescopes, Instruments, and Systems*, 1, 014003
- Rimmer, P. B., Xu, J., Thompson, S. J., et al. 2018, *Science Advances*, 4
- Rustamkulov, Z., Sing, D. K., Mukherjee, S., et al. 2023, *Nature*, 614, 659
- Scalo, J., Kaltenecker, L., Segura, A., et al. 2007, *Astrobiology*, 7, 85, copyright: Copyright 2018 Elsevier B.V., All rights reserved.
- Schmidt, S. P., MacDonald, R. J., Tsai, S.-M., et al. 2025, arXiv e-prints, arXiv:2501.18477
- Shields, A. L., Ballard, S., & Johnson, J. A. 2016, *Physics Reports*, 663, 1, the habitability of planets orbiting M-dwarf stars
- Shorttle, O., Jordan, S., Nicholls, H., Lichtenberg, T., & Bower, D. J. 2024, *ApJ*, 962, L8
- Tennyson, J. & Yurchenko, S. N. 2012, *MNRAS*, 425, 21
- Tsai, S.-M., Lee, E. K. H., Powell, D., et al. 2023, *Nature*, 617, 483
- Tsiaras, A., Waldmann, I. P., Tinetti, G., Tennyson, J., & Yurchenko, S. N. 2019, *Nature Astronomy*, 3, 1086
- Turrini, D., Schisano, E., Fonte, S., et al. 2021, *ApJ*, 909, 40
- Van Eylen, V., Agentoft, C., Lundkvist, M. S., et al. 2018, *MNRAS*, 479, 4786
- Veillet, R., Venot, O., Sirjean, B., et al. 2024, *A&A*, 682, A52
- Venot, O., Cavalié, T., Bounaceur, R., et al. 2020, *A&A*, 634, A78
- Venot, O., Hébrard, E., Agúndez, M., Decin, L., & Bounaceur, R. 2015, *A&A*, 577, A33
- Venot, O., Hébrard, E., Agúndez, M., et al. 2012, *A&A*, 546, A43
- Wogan, N. F., Batalha, N. E., Zahnle, K. J., et al. 2024, *ApJ*, 963, L7
- Youngblood, A., France, K., Loyd, R. O. P., et al. 2016, *ApJ*, 824, 101
- Yurchenko, S. N., Barber, R. J., & Tennyson, J. 2011, *MNRAS*, 413, 1828
- Yurchenko, S. N., Tennyson, J., & Bailey, J. e. a. 2014, *Proceedings of the National Academy of Science*, 111, 9379

Appendix A: Equilibrium chemistry retrieval results

In this appendix, we present all the results from the complementary retrieval assuming equilibrium chemistry. Although K2-18 b is expected to exhibit non-equilibrium chemistry, these results show that a single transit observed with NIRISS and NIRSpec G395H is insufficient to distinguish between equilibrium and non-equilibrium chemical states. This limitation arises from the lack of constraints on most species, with the exception of CH_4 , which is not strongly sensitive to non-equilibrium processes in K2-18 b's atmosphere.

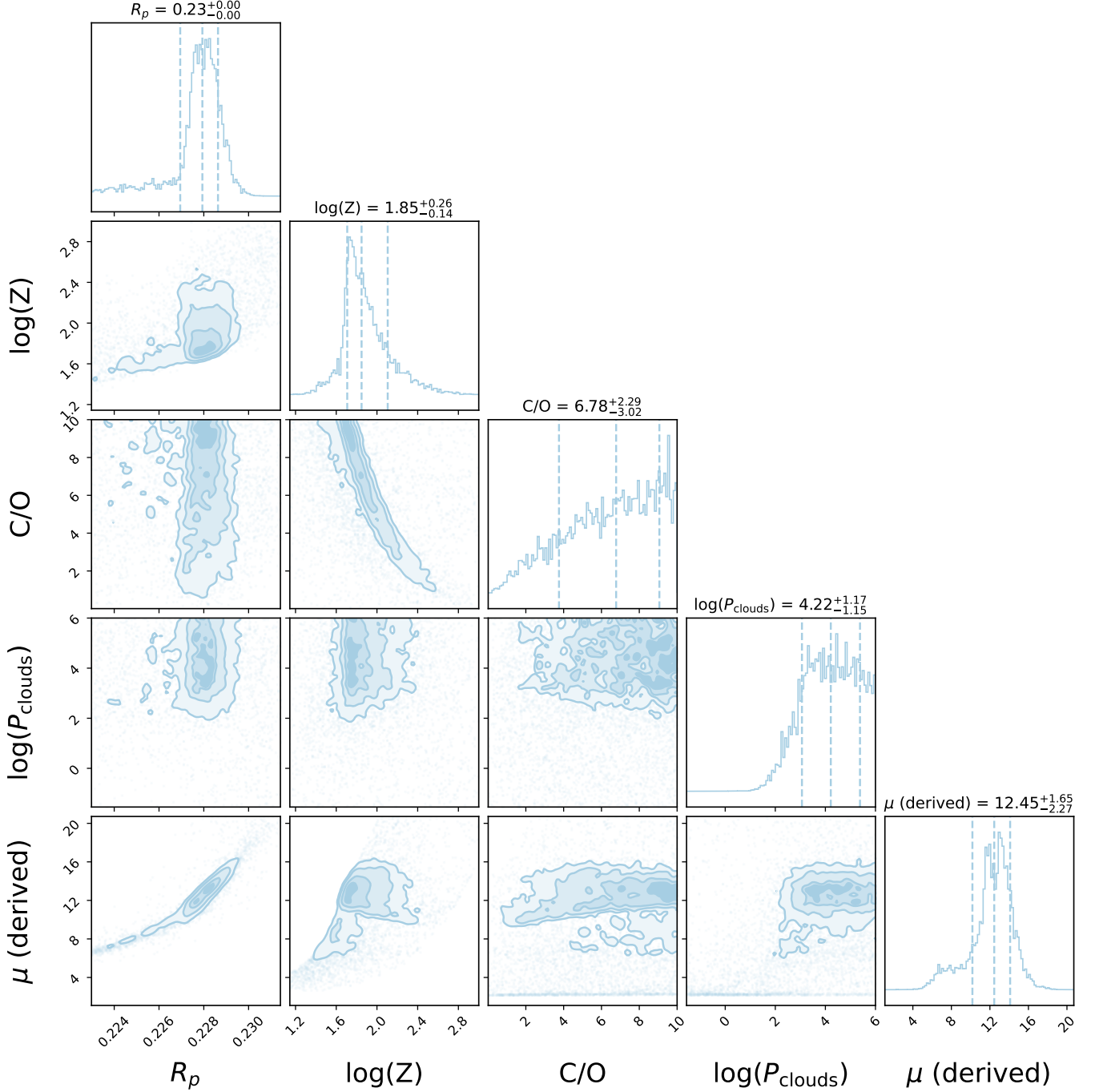


Fig. A.1: Posterior of the retrieval performed with equilibrium chemistry on the K2-18 b observation (Madhusudhan et al. 2023) native resolution with an offset of -41 ppm between NIRISS and NIRSpec data.

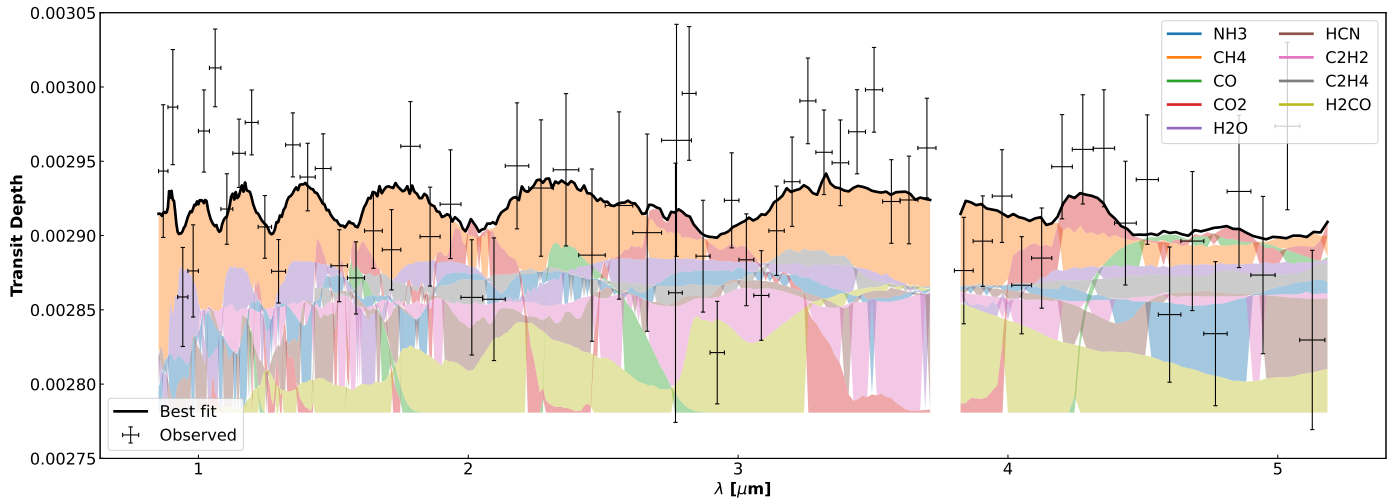


Fig. A.2: Transit spectra of the retrieved best fit equilibrium at resolution 200 (black solid line). It is compared to K2-18 b observation (Madhusudhan et al. 2023) low resolution representation with an offset of -41 ppm between NIRISS and NIRSPEC data. The contributions of considered molecules are represented with shaded colors.

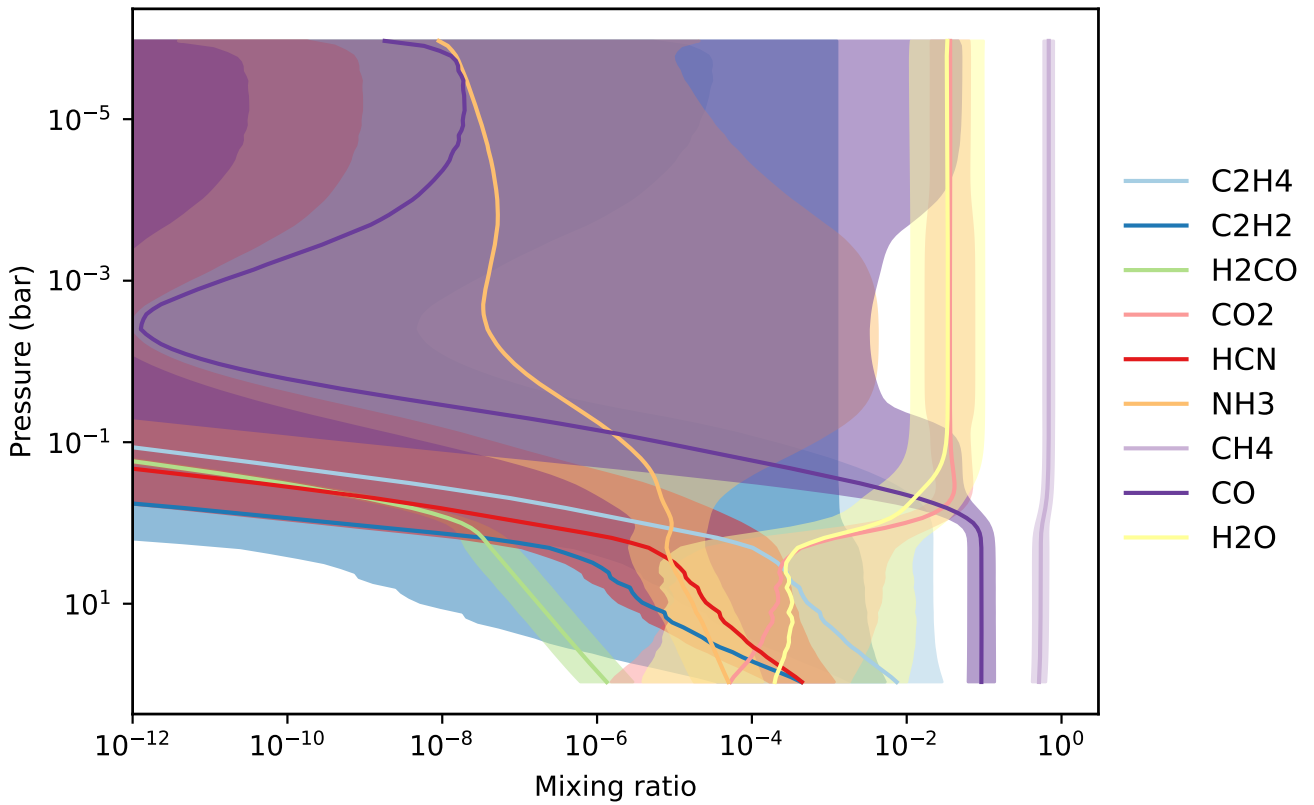


Fig. A.3: Species profiles of the retrieved best fit (solid line) with its uncertainty (shaded area).